Check for updates

Advanced Functional Materials

ADVANCED FUNCTIONAL MATERIALS
www.afm-journal.de

RESEARCH ARTICLE

The Intermolecular Long-Range Coupled Charge Transfer Excited State in $CsCu_2I_3$ Light-Emitting Diodes

Xiankan Zeng[1] | Yongjian Chen[3] | Lunyao Pan[4] | Maolin Mu[1] | Chenglong Li[1] | Xinning Wang[1] | Di Shen[1] | Jiasheng Xie[2] | Chenhao Deng[2] | Jianhao Ding[1] | Yujie Wen[1] | Shihai You[2] | Wen Li[1] | Weiqing Yang[1,2]

[1]School of Materials Science and Engineering, Key Laboratory of Advanced Technologies of Materials (Ministry of Education), Southwest Jiaotong University, Chengdu, People's Republic of China | [2]Research Institute of Frontier Science, Southwest Jiaotong University, Chengdu, People's Republic of China | [3]SEU-FEI Nano-Pico Center, School of Integrated Circuits, Key Lab of MEMS of Ministry of Education, Southeast University, Nanjing, People's Republic of China | [4]Key Laboratory of Electronic Thin Films and Integrated Devices, School of Optoelectronic Science and Engineering, University of Electronic Science and Technology of China, Chengdu, People's Republic of China

Correspondence: Wen Li (liwen3337@swjtu.edu.cn) | Weiqing Yang (wqyang@swjtu.edu.cn)

Received: 31 January 2026 | **Revised:** 21 July 2026 | **Accepted:** 23 July 2026

Keywords: cesium copper iodide | charge transfer | light-emitting diodes | long-coupled excited states | spacer layers

ABSTRACT

Low-dimensional ternary copper iodides are highly promising for future health displays and eco-friendly lighting due to their structural stability, excellent optoelectronic properties, high abundance, and low cost. However, the lack of a deep understanding of the complex charge transfer (CT) mechanism in their excited state dynamics hinders the efficiency progress of copper-based optoelectronic devices. Here, we provide a comprehensive analysis of the intermolecular CT excited-state dynamics in $CsCu_2I_3$ light-emitting diodes (LEDs) and demonstrate the long-range coupled characteristics of CT excitons. We report a strategy to achieve long-range coupled CT excited state by spatially separating electron-hole pairs, thereby enhancing the electroluminescence performance of $CsCu_2I_3$ LEDs. Carrier dynamics analysis reveals that the long-range coupled CT excited state achieves the highest delayed fluorescence contribution at the optimal coupling intensity, facilitating more efficient triplet energy harvesting. Accordingly, the $CsCu_2I_3$ LEDs exhibit a maximum external quantum efficiency of 4.3% and a peak luminance of 3666 cd/m^2, representing the highest luminance reported to date. Furthermore, the universality of the long-range coupled CT excited state has been demonstrated in other device structures. This study establishes a new method to pave the way for enhanced performance of $CsCu_2I_3$ LEDs toward practical applications.

1 | Introduction

Over the past decade, high-performance and low-cost solution-processed metal halide perovskite light-emitting diodes (PeLEDs) have greatly promoted research in next-generation displays and lighting [1–3]. The extraordinary breakthroughs in lead(Pb)-based PeLEDs have brought the external quantum efficiency (EQE) to a high level of 30%, showing strong momentum to catch up with commercial organic light-emitting diodes (OLEDs) [4–6]. However, the large-scale commercial production of lead-based PeLEDs is bound to face concerns about human health and environmental hazards caused by toxic lead elements [7]. Therefore, low-toxicity cations with similar structures, such as tin ions (Sn^{2+}) [8–10], cuprous ions (Cu^{+}) [11–13], and germanium ions (Ge^{2+}) [14, 15], have been widely developed to replace lead ions (Pb^{2+}) to effectively alleviate toxicity issues. Among them, one-dimensional (1D) ternary copper (Cu) halide $CsCu_2I_3$, with high structural stability, solution processing compatibility, and high-performance broadband warm white emission, have attracted lots of attention on the lead-free development path

All rights reserved, including rights for text and data mining and training of artificial intelligence technologies or similar technologies.
© 2026 Wiley-VCH GmbH

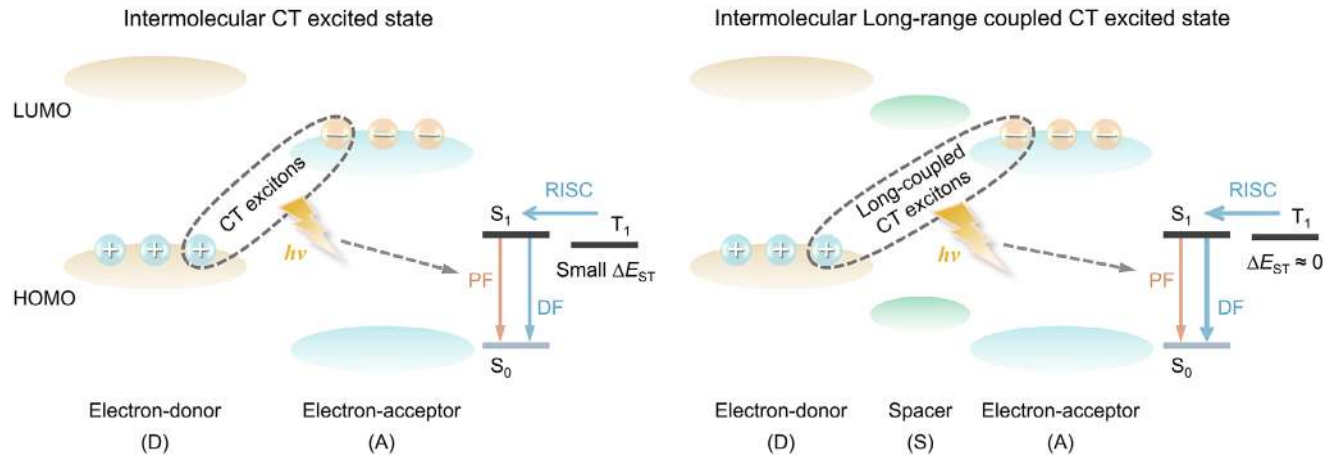


FIGURE 1 | Concept scheme of intermolecular CT excited state and long-range coupled CT excited state (PF: prompt fluorescence, DF: delayed fluorescence).

of PeLEDs [16–19]. Although the performance of $CsCu_2I_3$ LEDs has been optimized from multiple perspectives, such as additive engineering [11, 17, 20], buried interface modification [12, 19], and dipole layer design [21], there is still a gap compared to traditional Pb-based PeLEDs. The electron localization caused by the low-dimensional structure and the strong spin-orbit coupling (SOC) induced by the heavy Cu atoms lead to complex excited-state dynamics within the $CsCu_2I_3$ LEDs [22–25], and studies on it have never stopped. For instance, the distinct spectral response of excited states in the $CsCu_2I_3$ emission layer during PL and EL processes was attributed to carrier injection imbalance [26]. Besides, the interfacial copper iodide complex emission center induced by the charge transport layer was considered to be the origin of the low turn-on voltage in $CsCu_2I_3$ LEDs [16]. With the continuous deepening of research on copper iodide-based LEDs, these underlying charge transfer mechanisms urgently need to be clarified, and consensus on insights is required. Otherwise, it will restrict the further optimization of the performance of devices.

Here, we demonstrate the intermolecular charge transfer (CT) excited state between $CsCu_2I_3$ and electron transport material 1,3,5-tris (3-pyridyl-3-phenyl) benzene (TmPyPB) in $CsCu_2I_3$ LEDs. The systematic study on its photophysical properties and recombination dynamics has verified the long-range coupling characteristics of this CT excited state. 1,3-Dicarbazole-9-benzylbenzene (mCP), with bipolar transport property, is selected as a spacer to adjust the spatial separation distance of electron-hole pairs in the CT excited state. Under the optimal long-range coupling intensity, the intermolecular CT excitons exhibit an ultra-low energy gap between the singlet and triplet states (ΔE_{ST}) of 0.046 eV, and show a high thermally activated delayed fluorescence (TADF) contribution ratio of nearly 60% at room temperature. The significantly improved triplet energy harvesting efficiency endows the optimized $CsCu_2I_3$ LEDs with a 1.5-fold increase in EQE from 2.9% to 4.3% and a peak luminance of 3666 cd/m^2, which could be one of the few reported $CsCu_2I_3$ LEDs that can give consideration to both high luminance and high EQE. Furthermore, other electron transport layers and spacer layers are introduced to extend the research applicability, confirming the universality of constructing long-range coupled CT excitons to enhance the performance of $CsCu_2I_3$ LEDs. This work re-examines the understudied intermolecular CT mechanisms in $CsCu_2I_3$ LEDs and provides new insight into the decoupling of excited-state dynamics at the complex interface between heavy atom-based lead-free emission layers and transport layers.

2 | Results and Discussion

As shown in Figure 1, when an electron-donating (D) material with typical TADF luminescence characteristics comes into contact with a TADF-type electron-accepting (A) material, an intermolecular CT excited state can be formed, also known as an interfacial exciplex [27–30]. The frontier orbitals of this interfacial exciplex are separated onto D and A molecules, resulting in smaller orbital overlap integral between the highest occupied molecular orbital (HOMO) and the lowest unoccupied molecular orbital (LUMO). The D-A exciplex with significantly reduced electron-hole pair Coulomb force exhibits enhanced spin-orbit coupling (SOC) and narrowed ΔE_{ST}, representing a favourable TADF system. As a result, the high reverse intersystem crossing (RISC) process in the intermolecular CT excited state is accelerated, leading to efficient triplet energy harvesting [31–35]. Moreover, the long-range coupling effect enables the electron-hole pairs in CT excitons to maintain stable Coulomb interactions even when moderately separated by spacer (S) molecules with bipolar transport characteristics. The ΔE_{ST} of the long-coupled CT excited state is further narrowed to close to 0, leading to promoted RISC and maximized exciton utilization efficiency [36–39].

Similar intermolecular CT excitons are thought to dominate the excited states of $CsCu_2I_3$ LEDs. The high carrier migration capability of $CsCu_2I_3$ has been discussed in previous works [21, 23]. As shown in Figure S1a, there is a huge difference between the current density-voltage (*J-V*) curves of the single-carrier devices based on $CsCu_2I_3$. The hole-only device exhibits much larger current density compared to the electron-only device, demonstrating the charge-selective transport property of $CsCu_2I_3$, which is intrinsically caused by the effective mass difference between electron and hole [24, 40]. The self-trapped exciton (STE) configuration in $CsCu_2I_3$ causes electrons and holes to be localized at different positions in the crystal lattice, which

16163028, 2026, 71, Downloaded from https://advanced.onlinelibrary.wiley.com/doi/10.1002/adfm.77533 by Jilin University, Wiley Online Library on [07/11/2026]. See the Terms and Conditions (https://onlinelibrary.wiley.com/terms-and-conditions) on Wiley Online Library for rules of use; OA articles are governed by the applicable Creative Commons License

results in a significant decrease in the overlap of electron-hole wave functions, similar to the spatial separation of donors and acceptors in organic TADF materials. When $CsCu_2I_3$ is in contact with a common electron-accepting material, like 2,4,6-tris[3-(diphenylphosphinyl)phenyl]-1,3,5-triazine (PO-T2T), the emission peak shows a big redshift owing to the obvious charge transfer at the interface (Figure S1b). But for electron-donating material, such as tris(4-carbazoyl-9-ylphenyl)amine (TCTA), the redshift disappears, demonstrating the electron-donating characteristic of $CsCu_2I_3$. Combined with the ultraviolet photoelectron spectroscopy (UPS) and ultraviolet-visible spectroscopy (UV–vis), the energy level and bandgap (E_g) of $CsCu_2I_3$ and TmPyPB are determined (Figure S2). The energy band diagram of $CsCu_2I_3$/TmPyPB in the device is drawn in Figure S3. The energy difference between the valence band maximum (VBM) of $CsCu_2I_3$ and the LUMO of TmPyPB, as well as the energy difference between the conduction band minimum (CBM) of $CsCu_2I_3$ and the HOMO of TmPyPB, are both larger than 0.6 eV, which ensures that holes and electrons gather at the $CsCu_2I_3$/TmPyPB interface and form a stable intermolecular CT excited state. To gain insight into the frontier orbital configuration, the total density of states (TDOS) and partial density of states (PDOS) of $CsCu_2I_3$/TmPyPB were analyzed by density functional theory (DFT)-based first-principles calculations [23, 41]. As shown in Figure S4, the VBM is mainly composed of the hybrid orbitals of Cu 3d and I 5p, and the CBM is dominated not only by the electronic orbitals of Cu 4s and I 5p, but also by π electrons of C 2p orbitals from TmPyPB. To be clear, the $CsCu_2I_3$/TmPyPB structure studied here is not a simple small molecule surface adsorption model, but a typical Type-II heterojunction. Since the energy level difference between the CBM of $CsCu_2I_3$ and the LUMO of TmPyPB (0.7 eV) is smaller than the energy difference between VBM of $CsCu_2I_3$ and the HOMO of TmPyPB (1.1 eV), the electron cloud spatial interaction and electrostatic interaction between them cannot be ignored. The CBM orbital of $CsCu_2I_3$ and the LUMO orbital of TmPyPB will hybridize through the spatial interaction to form a new delocalized orbital [42, 43]. That is why the CBM calculated by DFT (ground states) is a hybrid orbital mixed with the CBM of $CsCu_2I_3$ and the LUMO orbital of TmPyPB. The remarkable electron cloud spatial interaction confirms the existence of spatially separated frontier orbitals at the $CsCu_2I_3$/TmPyPB interface.

Differences among the three excited states in $CsCu_2I_3$ (D), $CsCu_2I_3$/TmPyPB (D-A), and $CsCu_2I_3$/mCP/TmPyPB (D-S-A) are schematically shown in Figure 2a. The excited-state relaxation process of $CsCu_2I_3$ (D) is dominated by the intrinsic self-trapped exciton (STE) emission mechanism [22], while $CsCu_2I_3$/TmPyPB (D-A) tends to form spatially separated intermolecular CT excited states. The bipolar transport material mCP with appropriate energy levels was selected as a spacer molecule to achieve long-range coupling of CT excited states (Figure S5). By moderately adjusting the thickness of mCP (0–25 nm), the radiative recombination efficiency of long-range coupled CT excitons can be optimized. Spectroscopic characterizations were performed to analyze the differences in photophysical properties of the three excited states. The UV–vis and PL spectra of D, D-A, and D-S-A are exhibited in Figure 2b. The absorption peaks of the three samples are all located at 315 nm, indicating that the ground state electronic structures of the three samples are all dominated by the $CsCu_2I_3$ bulk phase. Compared with sample D, the D-A film shows a significantly enhanced PL intensity with a redshift of the emission peak, proving that when the ground state in D-A is excited, it tends to form a CT excited state with lower energy, structural stability, and higher recombination efficiency. The inserted mCP spacer properly lengthens the spatial separation distance of electron–hole pairs, resulting in weak electron coupling intensity and increased CT exciton energy, which is manifested as an obvious blueshift of the emission peak of sample D-S-A. D-S-A film exhibits the highest PL intensity among the three samples, indicating that the long-range coupled intermolecular CT excitons possess the most efficient radiative recombination. Here, the mCP spacer is designed into three thicknesses: S1, S2, and S3 (Figure S6), corresponding to small thickness (~3.4 nm), medium thickness (~11.6 nm), and large thickness (~22.7 nm). All "D-S-A" samples in the following represent sample D-S2-A with medium mCP thickness.

The UV–vis and PL spectra of D-S-A films with different mCP spacer thicknesses are exhibited in Figure S7a. As the mCP thickness increases, the PL spectra of the D-S-A films show a blueshift from 569 to 550 nm, indicating that the energy of the CT excited state is progressively enlarged by the spacer layer. In order to exclude the potential impact of charge transfer between D and S on the PL emission, PL spectra of D-S films with different spacer thicknesses were measured. With the increasing thickness, the films stably present a uniform emission peak at 558 nm (Figure S7b), demonstrating that the blueshift in PL spectra of the D-S-A films is entirely attributed to the increase in the CT excited state energy by the spacer-induced spatial separation. Besides, the absorption peaks show a negligible blueshift with the increase of mCP thickness, which can be ascribed to the weak rearrangement of the electron cloud at the $CsCu_2I_3$/mCP interface caused by the carbazole group of mCP. The unaffected E_g certifies that this interfacial interaction has little impact on the groundstate electronic structure of $CsCu_2I_3$ (Figure S8a).

The Urbach energy (E_U) values extracted from the UV-vis spectra of the three samples are shown in Figure 2c. Sample D-A exhibits a higher E_U compared to D, which is attributed to the high sensitivity of intermolecular CT exciton energy to interfacial dynamic disorder [44, 45]. The decrease in E_U of the D-S-A film indicates that the enlarged spatial separation distance of electron-hole pairs leads to a rapid attenuation of the electron coupling intensity in the CT excited state and the interaction between D and A, which reduces the structural disorder at the D-A interface and weakens the sensitivity of the CT exciton energy to local dynamic disorder. A consistent downward trend of E_U is observed in the E_U diagrams with increasing spacer thickness (Figure S8b,c).

Temperature-dependent PL spectroscopy was implemented to analyze the exciton binding energy (E_b) of the samples. All the samples show a consistent trend of PL intensity, first increasing and then decreasing as the temperature increased (Figure S9a–c). The interval in which the PL intensity monotonically decreases with temperature (178 to 298K) is selected for data fitting by the Arrhenius formula [46, 47].

As shown in Figure 2d, sample D-A shows a reduced E_b, indicating that the Coulomb attraction of the intermolecular CT excitons in D-A is weakened. The mCP spacer enlarges the

16163028, 2026, 71, Downloaded from https://advanced.onlinelibrary.wiley.com/doi/10.1002/adfm.77533 by Jilin University, Wiley Online Library on [07/11/2026]. See the Terms and Conditions (https://onlinelibrary.wiley.com/terms-and-conditions) on Wiley Online Library for rules of use; OA articles are governed by the applicable Creative Commons License

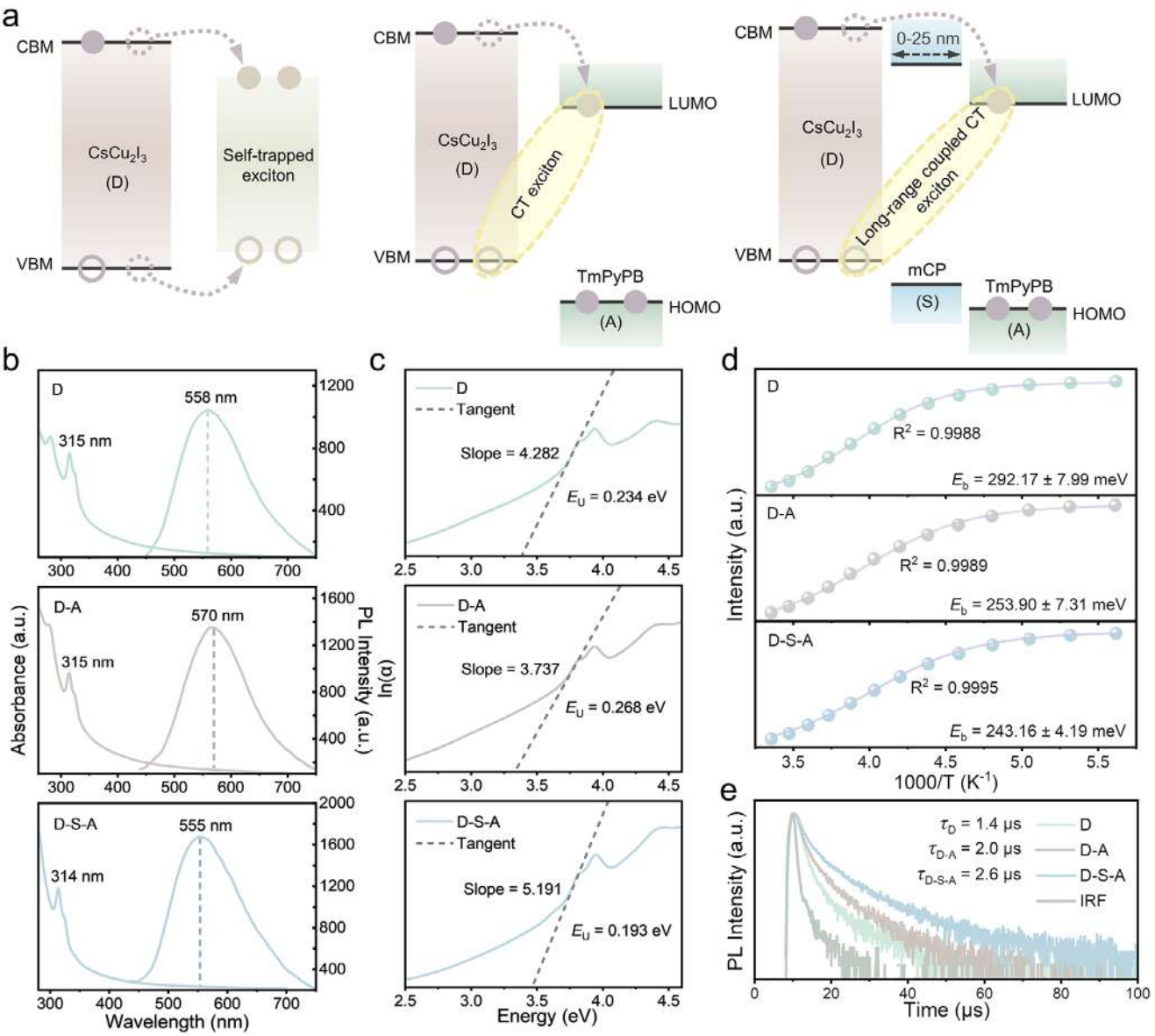


FIGURE 2 | Photophysical properties differences between the different excited states. (a) Schematic illustration of different charge transfer processes. (b) UV–vis and steady-state PL spectra (λ_{ex} = 260 nm), (c) Urbach energy diagrams, (d) integrated PL intensity as a function of 1000/T, (e) time-resolved PL decay curves of the samples with different excited states, as well as the instrument response function (IRF).

spatial separation of electron-hole pairs, resulting in a lower E_b (243.16meV). The time-resolved photoluminescence (TRPL) curves were fitted with a biexponential decay function [48]. As shown in Figure 2e, all the samples exhibit long lifetimes on the microsecond level, demonstrating that excited-state relaxation in all samples is dominated by the TADF process. Among them, D-A film exhibits increased average lifetime from 1.4 to 2.0 μs compared to sample D, indicating that the intermolecular CT excited state has a more efficient TADF process than the localized excited state (LE) in D. The D-S-A film shows the highest average lifetime (2.6 μs), indicating that the weakened electronic coupling intensity of CT excited states is beneficial to enhancing the exciton recombination efficiency. It can be seen from the TRPL spectra of samples with different thicknesses of mCP that the CT excitons of D-S2-A exhibit the longest decay lifetime (Figure S10a). The photoluminescence quantum yield (PLQY) data also demonstrate the highest radiative recombination efficiency in D-S2-A (Figure S10b,c). The detailed fitting parameters for TRPL spectra are summarized in Table S1. More details on the calculation of these fitting parameters can be seen in Figure S10.

In order to determine whether there are observable CT excited states between mCP and TmPyPB, the UV–vis and steady-state PL spectra of pure mCP, TmPyPB, and mCP/TmPyPB samples were further characterized. All the samples were synthesized under the same experimental conditions as the preparation of the D-S-A system. As shown in Figure S11a, the absorption spectrum of the mCP/TmPyPB mixed sample is very similar to that of the pure TmPyPB sample, with the main absorption peak located at ~260 nm, which can be attributed to the larger thickness of the TmPyPB layer dominating the absorption intensity. Although the thickness of mCP in the mixed film is very thin, the characteristic absorption peaks attributed to mCP at 296, 329, and 343 nm can still be observed, which proves the existence of mCP. Apart

16163028, 2026, 71, Downloaded from https://advanced.onlinelibrary.wiley.com/doi/10.1002/adfm.77533 by Jilin University, Wiley Online Library on [07/11/2026]. See the Terms and Conditions (https://onlinelibrary.wiley.com/terms-and-conditions) on Wiley Online Library for rules of use; OA articles are governed by the applicable Creative Commons License

from this, the absence of new absorption peaks, broadened peaks, and shifted peak positions indicates that there was no new ground-state transition in the mixed film. The PL spectra of the mixed film as well as the mCP and TmPyPB films are shown in Figure S11b. The mixed film was excited from both sides. For the sample excited from the mCP side (mCP/TmPyPB), it shows intrinsic double-peak emission consistent with mCP in the ultraviolet band (~ 350 nm). For the sample excited from the TmPyPB side (TmPyPB/mCP), it also shows intrinsic PL emission at 357 nm consistent with TmPyPB. Therefore, under the experimental conditions of the D-S-A system, a typical exciplex emission cannot be generated in the mCP/TmPyPB mixed film. This may be due to the incompatibility of the HOMO and LUMO energy levels of them, which hinders the complete formation of the exciplex. It demonstrates that the mCP/TmPyPB exciplex cannot be effectively formed in this D-S-A system and does not contribute to the blueshift of PL spectra and the improvement of fluorescence properties.

Temperature-dependent TRPL spectroscopy from 78 to 298 K was performed to study the joint contribution of phosphorescence (Phos) and TADF components to the decay lifetime of the three excited states (Figure 3a–c). The total PL decay lifetime (τ) can be fitted by the modified Boltzmann relation according to the following equation: [49–52]

$$\tau = \frac{3 + \exp\left(-\frac{\Delta E_{ST}}{k_B T}\right)}{\frac{3}{\tau_{T1}} + \frac{1}{\tau_{S1}} \exp\left(-\frac{\Delta E_{ST}}{k_B T}\right)}$$

where k_B represents the Boltzmann constant. The singlet and triplet lifetimes (τ_{S1} and τ_{T1}) and ΔE_{ST} can be obtained by fitting the τ vs. temperature curves with the above formula. Compared with D, sample D-A exhibits significantly increased τ_{S1} and τ_{T1}, and a reduced ΔE_{ST} from 0.083 to 0.076 eV (Figure 3d,e), indicating that the lower frontier orbital overlap in D-A disminishes the exchange energy and facilitates the proximity of the S_1 and T_1 energy levels. The ΔE_{ST} of sample D-S-A is further narrowed to 0.046 eV, endowing the long-range coupled CT excited state with the highest RISC efficiency (Figure 3f). The relative contribution ratio of Phos (I_{T1}/I) and TADF (I_{S1}/I) in the whole temperature window can be evaluated according to the following equations: [49, 50]

$$\frac{I_{T1}}{I} = \frac{1}{1 + \frac{\tau_{T1}}{3\tau_{S1}} \exp\left(-\frac{\Delta E_{ST}}{k_B T}\right)}$$

$$\frac{I_{S1}}{I} = 1 - \frac{I_{T1}}{I}$$

The fitting curves show that the exciton relaxation at low temperature is dominated by the Phos of the T_1 state (Figure 3g–i). With the increased temperature, the T_1 state returns to the S_1 state through an efficient RISC process and contributes to fluorescence emission in the form of TADF. Sample D-S-A exhibits the highest TADF emission fraction (f_{TADF}) of 59.1% at room temperature (298K), indicating that the smallest ΔE_{ST} helps achieve the best triplet energy harvesting efficiency. Similarly, the temperature-dependent TRPL measurements of the samples with different mCP thicknesses were also performed (Figure S12a,b). Compared with sample D-A, the incorporation of spacers with different thicknesses endows the CT excitons with noticeably reduced ΔE_{ST} and increased f_{TADF} (Figure S12c–f). Among them, the ΔE_{ST} of sample D-S3-A shows a small rebound to 0.054 eV, which is attributed to the increased probability of degradation back to the LE state by the weakened CT excited state characteristics induced by the excessively thick spacer. Therefore, an appropriate spacer layer thickness is crucial to improve the radiative recombination efficiency of the long-range coupled CT excited state in D-S-A. Furthermore, fundamental decay rates and time constants were calculated to evaluate the TADF behavior of the CT excited state. All of the constant values for D and D-S-A samples and their calculation details are summarized in Tables S2 and S3. The D-S2-A sample exhibits the fastest reverse intersystem crossing rate (k_{RISC}) by virtue of its smallest ΔE_{ST}, and the variation trend of k_{RISC} with the thickness of the spacer layer is consistent with other photophysical measurements mentioned above.

Femtosecond transient absorption spectroscopy (fs-TAS) was implemented to analyze the differences in excited-state dynamics of the three samples with a 320 nm pump pulse laser (Figure 4a–c). Rather rich spectral dynamics within the first 1 ps are shown in fs-TA spectra of sample D in Figure 4d: two characteristic absorption signal peaks at 465 and 520 nm are observed, one positive and one negative, corresponding to the excited state absorption (ESA) of STE and the bleaching of defect bound excitons (DBE), respectively. The rising DBE bleaching peak signal indicates that there is an intermediate state or trapping center induced by lattice defects during the formation of STE in $CsCu_2I_3$, which is considered to be the main cause of rapid non-radiative decay of sample D [22, 53, 54]. The DBE bleaching signal reaches its maximum intensity at approximately 1.4 ps and then gradually decays until it disappears at 52 ps, demonstrating that defect trapping is an ultrafast process, and the energy transfer process from DBE to STE is ongoing simultaneously. In addition, the ESA signal of sample D exhibits a redshift from 465 to 495 nm with the generation of DBE, which may be associated with the intrinsic structural relaxation of STE induced by the energy back-transfer of DBE. Similar ESA signal and no extra bleaching peaks are observed within the entire wavelength range of detection in both D-A and D-S-A films, indicating that the weak electronic coupling intensity of the CT excited state effectively suppresses the generation of sub-bandgap intermediate states caused by lattice distortion (Figure 4e,f). The rise rate of the ESA signal can reflect the ease of excited-state formation. The formation of LE in sample D relies on the electronic excitation and vibrational relaxation processes of the molecule itself, which is more time-consuming than the rapid charge transfer at the interface. Thus, its ESA signal rises at the slowest rate, reaching its maximum intensity at about 6 ps. After the ground state in D-A is excited, due to the close contact between D-A molecules, the excited-state electrons transfer to the LUMO of A at a fast speed, and the subsequent CT excited state is effectively formed in a very short time of 1.8 ps. Since the incorporated spacer layer increases the spatial distance and difficulty for excited-state electrons in D-S-A to transfer from D to A, resulting in an extended rise time of the ESA signals to 3.4 ps.

The ESA decay kinetics are fitted by a classic biexponential function that includes a fast decay component (τ_1) and a slow

16163028, 2026, 71, Downloaded from https://advanced.onlinelibrary.wiley.com/doi/10.1002/adfm.77533 by Jilin University, Wiley Online Library on [07/11/2026]. See the Terms and Conditions (https://onlinelibrary.wiley.com/terms-and-conditions) on Wiley Online Library for rules of use; OA articles are governed by the applicable Creative Commons License

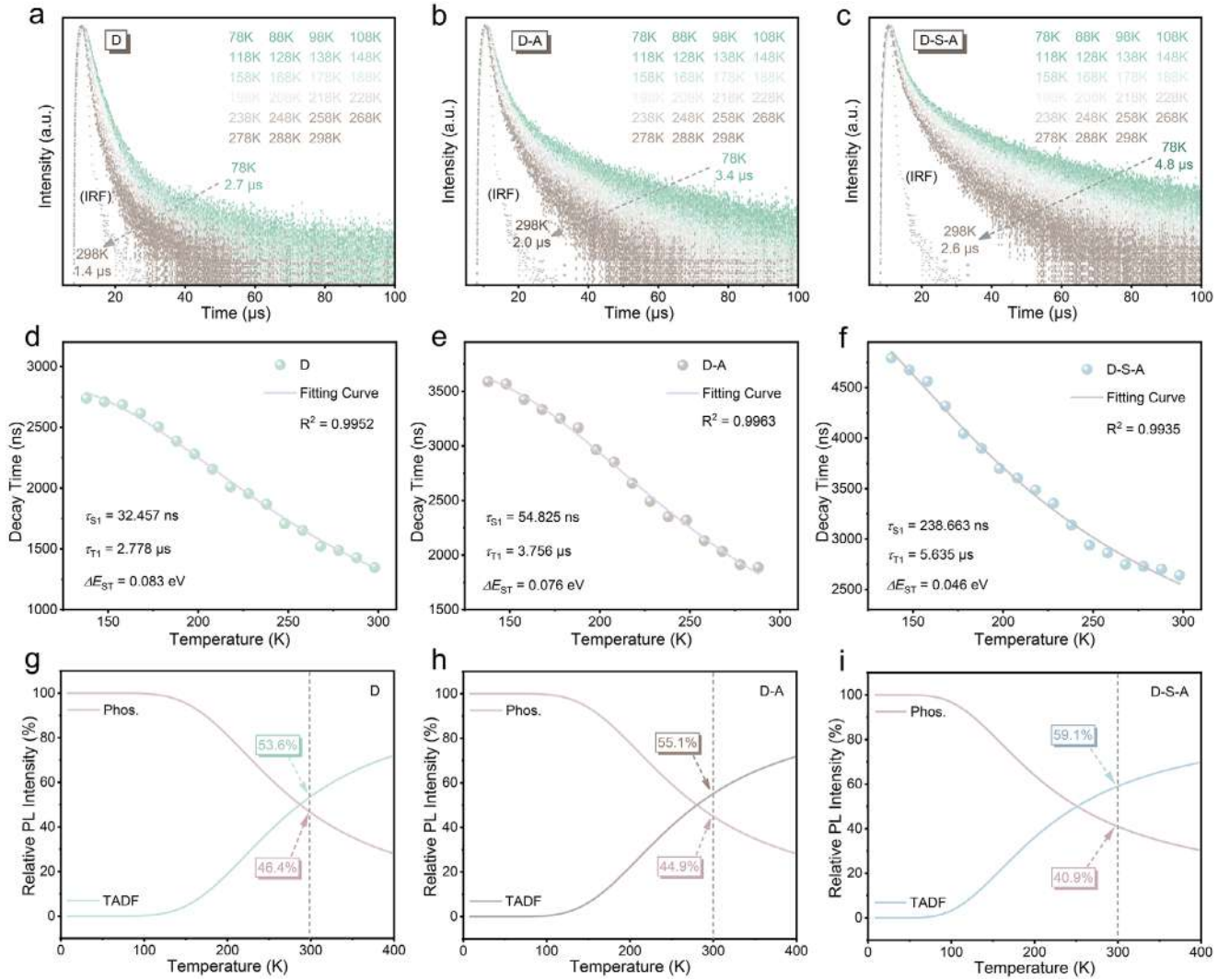


FIGURE 3 | TADF-phosphorescence dual-channel emission processes. PL decay curves varying with temperature from 78 to 298 K for (a) sample D, (b) sample D-A, (c) sample D-S-A. Average lifetime variation with temperature and corresponding fitting curves of (d) sample D, (e) sample D-A, (f) sample D-S-A. Simulation of temperature dependence of the fractional contributions of TADF and phosphorescence to the total emission in (g) sample D, (h) sample D-A, (i) sample D-S-A.

decay component (τ_2). The fast decay component corresponds to the excited-state quenching processes such as rapid non-radiative recombination, energy transfer, or charge separation, and the slow decay component reflects the long-lived radiative recombination relaxation paths of the excited state [55, 56]. The average lifetime of the excited state (τ_{ex}) can be calculated by the intensity-weighted average formula: $\tau_{ex} = (A_1 \cdot \tau_1^2 + A_2 \cdot \tau_2^2)/(A_1 \cdot \tau_1 + A_2 \cdot \tau_2)$. The detailed fitting data are displayed in the illustration of Figure 4g–i. Compared with sample D, the τ_{ex} of sample D-A is significantly increased from 516.92 to 617.43 ps, and the dominated fast decay contribution is effectively suppressed in D-A, demonstrating that the efficient recombination of the CT excited state alleviates the energy loss caused by the relaxation process of high-energy intermediate state in D. The long-range coupled CT excited state in D-S-A exhibits reduced non-radiative decay component due to the attenuated electronic coupling intensity. The extremely small ΔE_{ST} contributes to achieving the highest TADF recombination efficiency, thus realizing the longest τ_{ex} of 697.29 ps.

X-ray diffraction (XRD) was performed to analyze the effect of mCP on the crystallinity of $CsCu_2I_3$ films. The major diffraction peaks of the samples are consistently located at 26.09°, which correspond to the (221) crystal plane of orthorhombic $CsCu_2I_3$ (PDF#45-0076), indicating no disruption occurs to the lattice structure of $CsCu_2I_3$ in D-S films (Figure S13). The upper mCP layer with medium thickness endows the $CsCu_2I_3$ film with optimal crystallization quality, demonstrating that mCP with the S2 thickness is confirmed to derive optimal interaction with $CsCu_2I_3$. Atomic force microscopy (AFM) was further used to analyze the effect of the mCP spacer layer on the crystallization quality of the $CsCu_2I_3$ film. As shown in Figure S14, sample D-S2 shows the optimal morphology and the lowest surface roughness (Ra = 12.6 nm). As the thickness of the spacer layer increased to S3, the roughness increased sharply, indicating that only mCP with an appropriate thickness can exert the best crystallization control on the underlying $CsCu_2I_3$ film. X-ray photoelectron spectroscopy (XPS) was conducted to study the interlayer interaction between mCP and $CsCu_2I_3$. As shown in

16163028, 2026, 71, Downloaded from https://advanced.onlinelibrary.wiley.com/doi/10.1002/adfm.77533 by Jilin University, Wiley Online Library on [07/11/2026]. See the Terms and Conditions (https://onlinelibrary.wiley.com/terms-and-conditions) on Wiley Online Library for rules of use; OA articles are governed by the applicable Creative Commons License

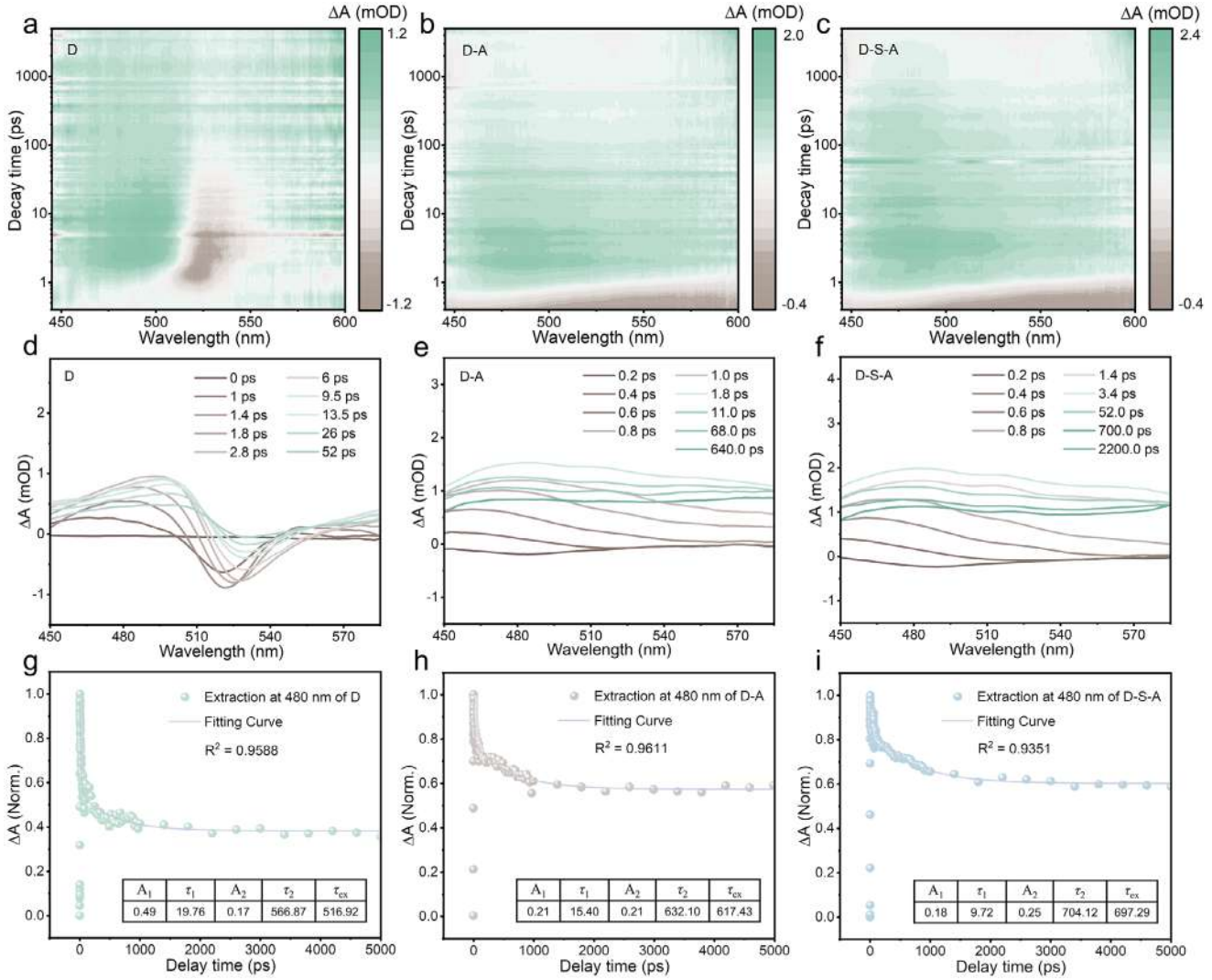


FIGURE 4 | Carrier dynamics of excited states. 2D color plot of fs-TAS of (a) sample D, (b) sample D-A, (c) sample D-S-A. fs-TAS spectra of (d) sample D, (e) sample D-A, (f) sample D-S-A. Normalized ESA decay kinetics of (g) sample D, (h) sample D-A, (i) sample D-S-A (The insets are the fitting data of the ESA decay kinetics; A1 and A2 represent the contribution coefficients of the fast decay and slow decay components, respectively).

Figure S15, when depositing mCP on $CsCu_2I_3$, the characteristic peaks of Cu 2p and I 3d shift toward higher binding energy. As the thickness of mCP increases, the degree of peak shift gets more evident. The large-scale peak shift exceeding 1.2 eV can be associated with the intensive charge transfer between mCP and $CsCu_2I_3$. The unique ambipolar transport property of mCP enables it to act as an electron acceptor to receive charges from the donor ($CsCu_2I_3$), laying the foundation for efficient charge transfer in the long-range coupled CT excited state in D-S-A.

$CsCu_2I_3$ LEDs are sequentially manufactured according to the multilayer structure of ITO/Poly(3,4-ethylenedioxythiophene):poly(styrenesulfonic acid) (PEDOT:PSS)/$CsCu_2I_3$/mCP/TmPyPB/LiF/Al (Figure 5a). To verify the effectiveness of the constructed long-coupled CT excited state, the overall performances of LEDs were evaluated by summarizing their electroluminescence (EL) characteristics. Current density-voltage-luminance (*J*–*V*–*L*) curves demonstrate that the luminance of all devices rises rapidly after the voltage exceeds 2.4 V (Figure 5b), and the D-S2-A device exhibits a maximum peak luminance of 3666 cd/m^2, which is the highest luminance reported in solution-processed $CsCu_2I_3$ LEDs to date. The normalized EL spectra under a voltage of 4.0 V were extracted to compare the spectral response dependence of the long-range coupled CT excited state on the spacer thickness (Figure 5c). The D-S0-A device exhibits a broadband warm-white light emission at 564 nm and a distinct blueshift for the EL peaks with the increase of the mCP thickness, which is consistent with the PL spectra in Figure S7a and can be attributed to the decrease in Coulomb attraction energy of electron-hole pairs [36, 37].

As shown in Figure 5d, the D-S2-A device exhibits the highest peak EQE of 4.3%, which is 1.5 times higher than that of the device without spacer (D-S0-A), demonstrating that an appropriate spatial separation distance in the CT excited state can definitely promote the maximization of radiation recombination efficiency. Detailed performance parameters for the device are summarized in Table S4. Twenty devices with different spacer layer thicknesses were prepared for the robustness test of EQE

16163028, 2026, 71, Downloaded from https://advanced.onlinelibrary.wiley.com/doi/10.1002/adfm.77533 by Jilin University, Wiley Online Library on [07/11/2026]. See the Terms and Conditions (https://onlinelibrary.wiley.com/terms-and-conditions) on Wiley Online Library for rules of use; OA articles are governed by the applicable Creative Commons License

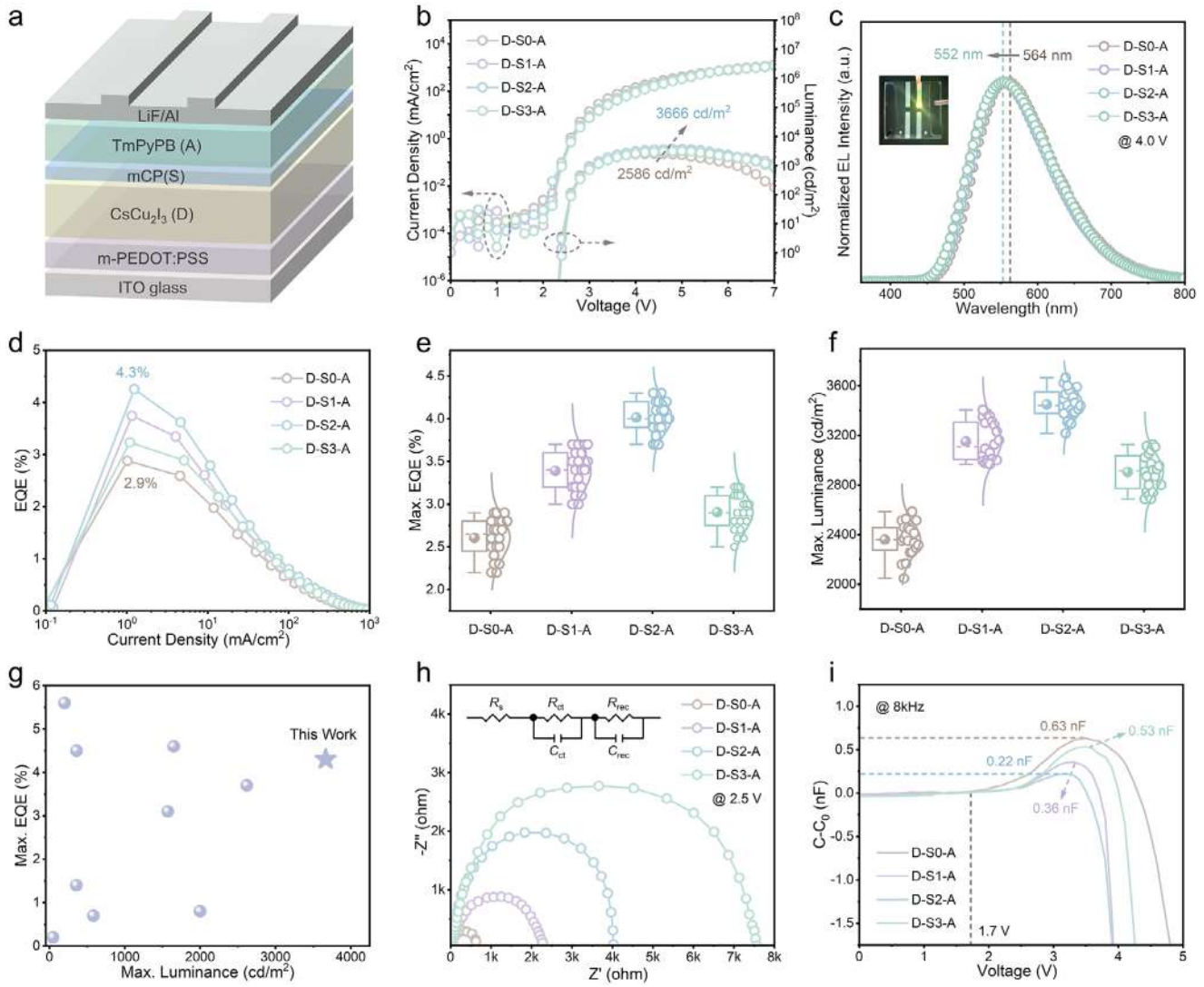


FIGURE 5 | Characterization of $CsCu_2I_3$ LEDs with different spacer layer thicknesses. (a) Schematic illustration of $CsCu_2I_3$ LEDs with multiple heterostructures. (b) *J–V–L* curves, (c) normalized EL spectra (the inset is the emitting photograph of D-S2-A device with a 4 mm^2 active area), (d) EQE-current density curves, (e) the peak EQE statistical distribution and (f) the peak luminance statistical distribution of the D-S-A devices with different thicknesses of S. (g) Device performance comparison of this work with other reported solution-processed $CsCu_2I_3$ LEDs. (h) Nyquist plots by EIS measurements under a bias voltage of 2.5 V and (i) capacitance variation vs. voltage curves at 8 kHz of the devices.

and luminance. The statistical distribution box plots of peak EQE and peak luminance are shown in Figure 5e,f. The D-S2-A device exhibits an average peak EQE of 4.0% and an peak average luminance of 3443 cd/m^2, indicating that the strategy of constructing long-range coupled CT excited state to enhance the performance of $CsCu_2I_3$ LEDs has good reproducibility. The half lifetime (T_{50}) of the $CsCu_2I_3$ LEDs was measured by applying a constant voltage and monitoring the luminance change curve. The classical T_{50} is defined as the time it takes for luminance to decay from 100 cd/m^2 to half at a constant bias voltage. As shown in Figure S16, the D-S2-A device exhibits the best T_{50}, verifying that the long-range coupling effect of CT excited states at an appropriate distance can greatly improve the exciton recombination efficiency and help the device to achieve the highest EL performance. The reported peak EQE and peak luminance data for solution-processed $CsCu_2I_3$ LEDs are summarized in Figure 5g. This work achieves a good balance between high luminance and high EQE by manipulating long-range coupled CT excited state in $CsCu_2I_3$ LEDs. The relevant parameters of these reported $CsCu_2I_3$ LEDs are presented in Table S5.

Electrochemical impedance spectroscopy (EIS) and capacitance-voltage (*C-V*) characteristic curves were implemented to analyze the carrier transport and recombination dynamics of the devices. A simplified equivalent circuit model was used to fit the Nyquist plots, as shown in the inset of Figure 5h, the circuit consists of five components: series resistance (R_s), charge transfer resistance (R_{ct}), charge transfer capacitance (C_{ct}), recombination resistance (R_{rec}), and recombination capacitance (C_{rec}). Among them, R_{ct} can indirectly reflect the difficulty of the interface CT excited-state formation in the devices, and R_{rec} is negatively correlated with the radiative recombination efficiency of the CT excited state [21, 57]. All the detailed fitting data are shown in Table S6. A constant increasing trend of R_{ct} is observed with the spacer thickness increasing, which can be associated with the enlarged cross-interface tunneling distance of carriers and accordingly

16163028, 2026, 71, Downloaded from https://advanced.onlinelibrary.wiley.com/doi/10.1002/adfm.77533 by Jilin University, Wiley Online Library on [07/11/2026]. See the Terms and Conditions (https://onlinelibrary.wiley.com/terms-and-conditions) on Wiley Online Library for rules of use; OA articles are governed by the applicable Creative Commons License

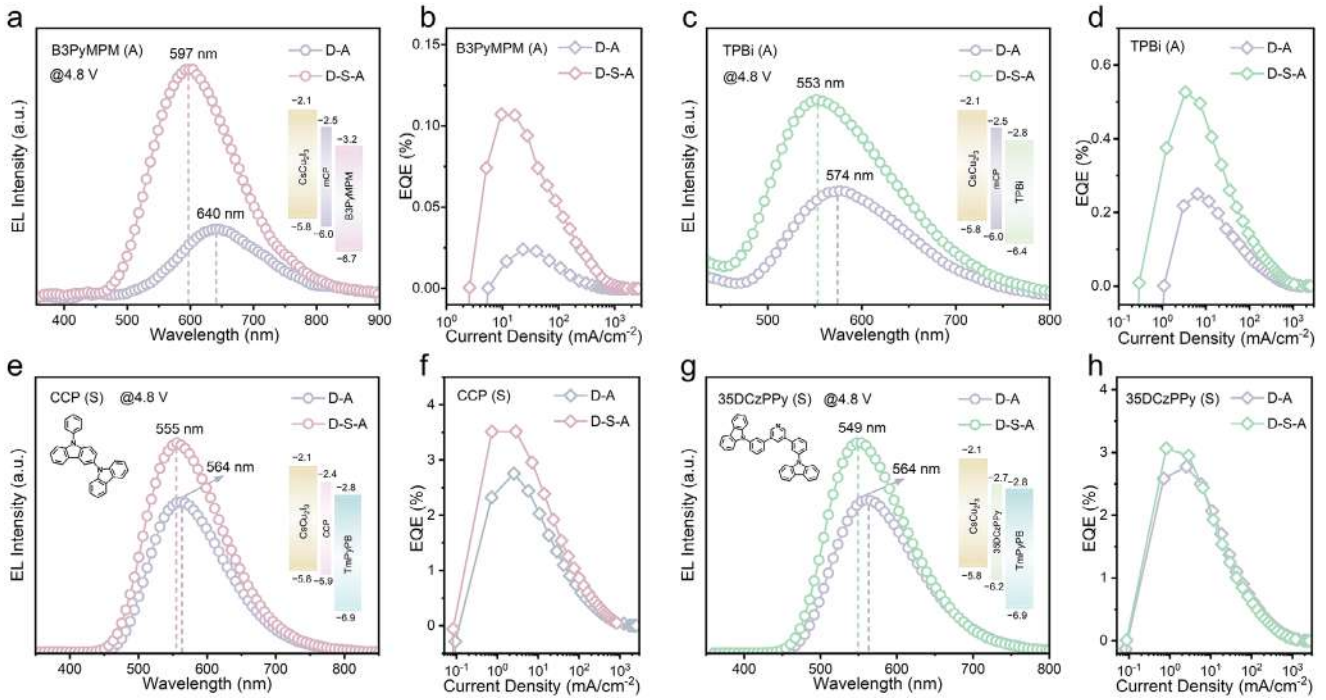


FIGURE 6 | The universality expansion of long-range coupled CT excitons in $CsCu_2I_3$ LEDs. (a) EL spectra under a bias voltage of 4.8 V and (b) EQE-current density curves of B3PyMPM-based devices without or with mCP spacer. (c) EL spectra under a bias voltage of 4.8 V and (d) EQE-current density curves of TPBi-based devices without or with mCP spacer. (e) EL spectra under a bias voltage of 4.8 V and (f) EQE-current density curves of CCP-based devices without or with spacer. (g) EL spectra under a bias voltage of 4.8 V and (h) EQE-current density curves of 35DCzPPy-based devices without or with spacer.

increased activation energy to form long-range coupled CT excitons. The trend of R_{rec} initially declined and then rose, realizing its maximum value in the D-S2-A device, indicating that there is an optimal thickness window for the spacer layer. The appropriate thickness can endow the CT excited state with the smallest ΔE_{ST}, ultimately maximizing the radiative recombination efficiency. In short, the spacer layer sacrifices part of the carrier injection and transfer speed in exchange for the optimization of the excited state and a leap in radiative recombination efficiency. The *C*–*V* characteristic curves at low frequency can more clearly reflect the differences in carrier transfer behavior during device operation [21, 58]. To make the data more intuitive, the *C*–*V* curves were initialized (Figure 5i). The D-S0-A device starts charge transfer at a low voltage (1.7 V) and ultimately shows a capacitance increment of 0.63 nF, indicating that the interlayer charge transfer barrier is smaller in D-A devices without spacer layers, allowing for more rapid and earlier charge transfer and accumulation. In the D-S-A device, the increasein the spatial separation distance between D and A molecules results in a smoother and more controllable accumulation process of the unbalanced charges at the D-A interface. The low capacitance variation of 0.22 nF reflects that charge accumulation at the D-A interface is effectively suppressed, which helps reduce carrier non-radiative losses and improve exciton utilization efficiency.

To verify the universality of long-range coupled CT excitons in $CsCu_2I_3$ LEDs, other electron donor materials were chosen to fabricate D-S-A devices. The EL performance and EQE-current density curves of the devices are shown in Figure 6a–d. The D-S-A devices based on 4,6-bis(3,5-bis(3-pyridylphenyl)-2-methylpyrimidine (B3PyMPM) and 1,3,5-tris(1-phenyl-1H-benzimidazol-2-yl)benzene (TPBi) both exhibit a similar blueshift in the EL spectra, indicating that the energy of long-range coupled CT excitons is effectively enhanced by the spacer layer. The EQE of these D-S-A devices is significantly improved by 4.5 times in D-S-B3PyMPM and by 2 times in D-S-TPBi, demonstrating that the long-range coupled CT excitons are universal in $CsCu_2I_3$ LEDs with different device architectures.

To further expand the applicability of long-range coupling CT excitons, two additional carbazole molecules with high triplet energy were selected as spacer layers to fabricate D-S-A devices. Both N-phenyl-9H-3,9'-dicarbazole (CCP) and 3,5-bis(3-(9H-carbazol-9-yl)phenyl)pyridine (35DCzPPy) contain carbazole groups capable of electrostatic interaction with $CsCu_2I_3$, ensuring the stability of the D-S-A excited state. The molecular structural formulas and corresponding D-S-A energy level diagrams are shown in the insets of Figure 6e,g. The EL spectra of both D-S-A devices exhibit a recognizable blueshift, and the EQE of the devices shows an effective improvement (Figure 6e,h), indicating that carbazole-based TADF molecules with high triplet energy are universally applicable as a spacer for the CT excited state in $CsCu_2I_3$ LEDs. Detailed performance of these extended devices is summarized in Table S7.

3 | Conclusion

In summary, the overlooked intermolecular CT excited state dynamics in $CsCu_2I_3$ LEDs deserve to be re-examined thought-

16163028, 2026, 71, Downloaded from https://advanced.onlinelibrary.wiley.com/doi/10.1002/adfm.77533 by Jilin University, Wiley Online Library on [07/11/2026]. See the Terms and Conditions (https://onlinelibrary.wiley.com/terms-and-conditions) on Wiley Online Library for rules of use; OA articles are governed by the applicable Creative Commons License

fully. This work has successfully covered a comprehensive understanding of the recombination dynamics for long-range coupled CT excitons commonly observed in $CsCu_2I_3$ LEDs. By rationally designing the spacer thickness, we have implemented the spatial optimization of the long-range coupled CT excited state, maximizing the exciton radiative recombination efficiency. The optimal $CsCu_2I_3$ LEDs achieved a peak EQE of 4.3% and a maximum luminance of 3666 cd/m^2, representing the highest luminance among solution-processed $CsCu_2I_3$ LEDs to date. Our work pioneers the study of the intermolecular CT excited states in PeLEDs and provides a new insight into improving the triplet energy harvesting efficiency from the perspective of optimizing the spatial configuration of excited states.

Author Contributions

Xiankan Zeng: conceptualization, methodology, software, writing – original draft, writing – review and editing, formal analysis, validation, data curation, investigation, project administration. **Yongjian Chen**: methodology, formal analysis, conceptualization. **Lunyao Pan**: investigation, validation, supervision. **Maolin Mu**: investigation, funding acquisition. **Chenglong Li**: funding acquisition, investigation. **Xinning Wang**: validation, investigation. **Di Shen**: investigation, validation. **Jiasheng Xie**: supervision, validation. **Chenhao Deng**: validation, methodology. **Jianhao Ding**: investigation, validation. **Yujie Wen**: investigation, validation. **Shihai You**: methodology, conceptualization, resources. **Wen Li**: funding acquisition, writing – review and editing, conceptualization, methodology, resources, supervision. **Weiqing Yang**: writing – review and editing, conceptualization, methodology, funding acquisition, resources.

Acknowledgements

We acknowledge the financial support from the National Natural Science Foundation of China (No. 52202188). The authors would like to thank the Analysis and Testing Center of Southwest Jiaotong University for supporting the ellipsometric measurements. The authors gratefully acknowledge Ceshigo Research Service and Zhongkebaice Technology Service Co., Ltd. for providing XPS, UPS, and TAS testing services.

Conflicts of Interest

The authors declare no conflicts of interest.

Data Availability Statement

The data that support the findings of this study are available from the corresponding author upon reasonable request.

References

1. T.-H. Han, K. Y. Jang, Y. Dong, R. H. Friend, E. H. Sargent, and T.-W. Lee, "A Roadmap for the Commercialization of Perovskite Light Emitters," *Nature Reviews Materials* 7 (2022): 757–777, https://doi.org/10.1038/s41578-022-00459-4.

2. X.-K. Liu, W. Xu, S. Bai, et al., "Metal Halide Perovskites for Light-Emitting Diodes," *Nature Materials* 20 (2021): 10–21, https://doi.org/10.1038/s41563-020-0784-7.

3. M. Zhang, X. Ma, J. L. Esguerra, et al., "Towards Sustainable Perovskite Light-Emitting Diodes," *Nature Sustainability* 8 (2025): 315–324, https://doi.org/10.1038/s41893-024-01503-7.

4. Z. Xing, G. Jin, Q. Du, et al., "Ions-induced Assembly of Perovskite Nanocomposites for Highly Efficient Light-Emitting Diodes With EQE Exceeding 30%," *Advanced Materials* 36 (2024): 2406706, https://doi.org/10.1002/adma.202406706.

5. J. Jiang, Z. Xia, M. Shi, et al., "Efficient Red Perovskite LEDs With Iodine Management via Volatile Additive I_2," *Advanced Materials* 37 (2025): 2503699, https://doi.org/10.1002/adma.202503699.

6. Y. Gao, Q. Cai, Y. He, et al., "Highly Efficient Blue Light-Emitting Diodes Based on Mixed-Halide Perovskites With Reduced Chlorine Defects," *Science Advances* 10 (2024): ado5645, https://doi.org/10.1126/sciadv.ado5645.

7. A. L. Wani, A. Ara, and J. A. Usmani, "Lead Toxicity: A Review," *Interdisciplinary Toxicology* 8 (2015): 55–64, https://doi.org/10.1515/intox-2015-0009.

8. F. Yuan, G. Folpini, T. Liu, et al., "Bright and Stable Near-Infrared Lead-Free Perovskite Light-Emitting Diodes," *Nature Photonics* 18 (2024): 170–176, https://doi.org/10.1038/s41566-023-01351-5.

9. X.-Z. Li, Y. Ye, Y. Cao, et al., "Tin-Halide Perovskites for Light-Emitting Diodes," *Chemical Society Reviews* 54 (2025): 6697–6725, https://doi.org/10.1039/D5CS00340G.

10. Q. Teng, Q. Tan, M. Hou, J. Zhang, and F. Yuan, "Binary Host-Guest Strategy Enables Bright and Efficient Lead-Free Zero-Dimensional Tin Halide Light-Emitting Diodes," *Science Advances* 11 (2025): adw5454, https://doi.org/10.1126/sciadv.adw5454.

11. H. Chen, L. Zhu, C. Xue, et al., "Efficient and Bright Warm-White Electroluminescence From Lead-Free Metal Halides," *Nature Communications* 12 (2021): 1421, https://doi.org/10.1038/s41467-021-21638-x.

12. C. Zhuo, C. Wang, P. Xie, et al., "Regulation of Additive-Cs^+ Interactions for Efficient Cesium Copper Iodide Light-Emitting Diodes," *ACS Photonics* 12 (2025): 1227–1234.

13. X. Liu, F. Yuan, C. Zhu, et al., "Near-Unity Blue Luminance From Lead-Free Copper Halides for Light-Emitting Diodes," *Nano Energy* 91 (2022): 106664, https://doi.org/10.1016/j.nanoen.2021.106664.

14. D. Yang, G. Zhang, R. Lai, et al., "Germanium-Lead Perovskite Light-Emitting Diodes," *Nature Communications* 12 (2021): 4295, https://doi.org/10.1038/s41467-021-24616-5.

15. Y. Zhou, C. Zou, D. Peng, et al., "Reduced-Toxicity and Highly Luminescent Germanium–Lead Perovskites Enabled by Strain Reduction for Light-Emitting Diodes," *The Journal of Physical Chemistry Letters* 15 (2024): 6443–6450, https://doi.org/10.1021/acs.jpclett.4c01478.

16. R. Xu, D. Zhang, J. Si, et al., "Low-Voltage Driving Copper Iodide-Based Broadband Electroluminescence," *ACS Energy Letters* 7 (2022): 4408–4416, https://doi.org/10.1021/acsenergylett.2c02471.

17. Z. Ma, X. Ji, M. Wang, et al., "Carbazole-Containing Polymer-Assisted Trap Passivation and Hole-Injection Promotion for Efficient and Stable $CsCu_2I_3$ -Based Yellow LEDs," *Advanced Science* 9 (2022): 2202408, https://doi.org/10.1002/advs.202202408.

18. G. Seo, H. Jung, T. D. Creason, et al., "Lead-Free Halide Light-Emitting Diodes With External Quantum Efficiency Exceeding 7% Using Host–Dopant Strategy," *ACS Energy Letters* 6 (2021): 2584–2593, https://doi.org/10.1021/acsenergylett.1c01117.

19. N. Zhao, J. Yan, C. Zhuo, et al., "Enhanced Charge Balance for Efficient Electroluminescence From Cesium Copper Halides," *The Journal of Physical Chemistry Letters* 14 (2023): 6867–6871, https://doi.org/10.1021/acs.jpclett.3c01821.

20. S. Yang, Z. Tang, B. Qu, L. Xiao, and Z. Chen, "Crown-Assisted $CsCu_2I_3$ Growth and Trap Passivation for Perovskite Light-Emitting Diodes," *ACS Applied Materials & Interfaces* 16 (2024): 20776–20785.

21. X. Zeng, Q. Yin, L. Pan, et al., "Hole Delayed-Release Effect of Inorganic Interfacial Dipole Layer on Charge Balance for Boosting $CsCu_2I_3$ Light-Emitting Diodes," *ACS Nano* 19 (2025): 11878–11890, https://doi.org/10.1021/acsnano.4c14429.

22. R. Kentsch, M. Morgenroth, M. Scholz, et al., "Direct Observation of the Exciton Self-Trapping Process in $CsCu_2I_3$ Thin Films," *The Journal of Physical Chemistry Letters* 11 (2020): 4286–4291, https://doi.org/10.1021/acs.jpclett.0c01130.

16163028, 2026, 71, Downloaded from https://advanced.onlinelibrary.wiley.com/doi/10.1002/adfm.77533 by Jilin University, Wiley Online Library on [07/11/2026]. See the Terms and Conditions (https://onlinelibrary.wiley.com/terms-and-conditions) on Wiley Online Library for rules of use; OA articles are governed by the applicable Creative Commons License

23. Z. Li, Z. Li, Z. Shi, and X. Fang, "Facet-Dependent, Fast Response, and Broadband Photodetector Based on Highly Stable All-Inorganic $CsCu_2I_3$ Single Crystal With 1D Electronic Structure," *Advanced Functional Materials* 30 (2020): 2002634, https://doi.org/10.1002/adfm.202002634.

24. Y. Hui, S. Chen, R. Lin, W. Zheng, and F. Huang, "Photophysics in $Cs_3Cu_2I_5$ and $CsCu_2I_3$," *Materials Chemistry Frontiers* 5 (2021): 7088–7107, https://doi.org/10.1039/D1QM00552A.

25. M.-H. Du, "Emission Trend of Multiple Self-Trapped Excitons in Luminescent 1D Copper Halides," *ACS Energy Letters* 5 (2020): 464–469, https://doi.org/10.1021/acsenergylett.9b02688.

26. U. M. Kuruppu, M. A. Rahman, and M. K. Gangishetty, "Unraveling the Origin of an Unusual Shift in the Electroluminescence of 1D $CsCu_2I_3$ Light-Emitting Diodes," *ACS Nano* 18 (2024): 1647–1657, https://doi.org/10.1021/acsnano.3c09824.

27. Y. Tao, K. Yuan, T. Chen, et al., "Thermally Activated Delayed Fluorescence Materials Towards the Breakthrough of Organoelectronics," *Advanced Materials* 26 (2014): 7931–7958, https://doi.org/10.1002/adma.201402532.

28. S. Y. Byeon, D. R. Lee, K. S. Yook, and J. Y. Lee, "Recent Progress of Singlet-Exciton-Harvesting Fluorescent Organic Light-Emitting Diodes by Energy Transfer Processes," *Advanced Materials* 31 (2019): 1803714, https://doi.org/10.1002/adma.201803714.

29. J. Gu, Z. Tang, H. Guo, et al., "Intermolecular TADF: Bulk and Interface Exciplexes," *Journal of Materials Chemistry C* 10 (2022): 4521–4532, https://doi.org/10.1039/D1TC04950J.

30. M. Sarma, L.-M. Chen, Y.-S. Chen, and K.-T. Wong, "Exciplexes in OLEDs: Principles and Promises," *Materials Science and Engineering: R: Reports* 150 (2022): 100689, https://doi.org/10.1016/j.mser.2022.100689.

31. T. Zhang, B. Chu, W. Li, et al., "Efficient Triplet Application in Exciplex Delayed-Fluorescence OLEDs Using a Reverse Intersystem Crossing Mechanism Based on a Δ ES–T of Around Zero," *ACS Applied Materials & Interfaces* 6 (2014): 11907–11914, https://doi.org/10.1021/am501164s.

32. M. Sarma and K.-T. Wong, "Exciplex: An Intermolecular Charge-Transfer Approach for TADF," *ACS Applied Materials & Interfaces* 10 (2018): 19279–19304, https://doi.org/10.1021/acsami.7b18318.

33. D. Yang, J.-M. Kim, J.-S. Huh, J.-J. Kim, and J.-I. Hong, "The Effect of the Electron-Donor Ability on the OLED Efficiency of Twisted Donor-Acceptor Type Emitters," *Organic Electronics* 95 (2021): 106187, https://doi.org/10.1016/j.orgel.2021.106187.

34. W.-Y. Hung, P.-Y. Chiang, S.-W. Lin, et al., "Balance the Carrier Mobility To Achieve High Performance Exciplex OLED Using a Triazine-Based Acceptor," *ACS Applied Materials & Interfaces* 8 (2016): 4811–4818, https://doi.org/10.1021/acsami.5b11895.

35. K.-H. Kim, S.-J. Yoo, and J.-J. Kim, "Boosting Triplet Harvest by Reducing Nonradiative Transition of Exciplex Toward Fluorescent Organic Light-Emitting Diodes With 100% Internal Quantum Efficiency," *Chemistry of Materials* 28 (2016): 1936–1941, https://doi.org/10.1021/acs.chemmater.6b00478.

36. P. Yuan, X. Guo, X. Qiao, D. Yan, and D. Ma, "Improvement of the Electroluminescence Performance of Exciplex-Based OLEDs by Effective Utilization of Long-Range Coupled Electron–Hole Pairs," *Advanced Optical Materials* 7 (2019): 1801648, https://doi.org/10.1002/adom.201801648.

37. H. Nakanotani, T. Furukawa, K. Morimoto, and C. Adachi, "Long-Range Coupling of Electron-Hole Pairs in Spatially Separated Organic Donor-Acceptor Layers," *Science Advances* 2 (2016): 1501470.

38. B. Dong, J. Yan, G. Li, et al., "High Luminance/Efficiency Monochrome and White Organic Light Emitting Diodes Based Pure Exciplex Emission," *Organic Electronics* 106 (2022): 106528, https://doi.org/10.1016/j.orgel.2022.106528.

39. J. Wang, T. Pan, D. Zhang, H. Yang, G. Wang, and L. Zhou, "Enhanced Efficiency and Delayed Decay of Organic Light-Emitting Diodes by Incorporating Spacer Layer Based on Low-Triplet Energy Interfacial Exciplex," *The Journal of Physical Chemistry C* 129 (2025): 764–773, https://doi.org/10.1021/acs.jpcc.4c06784.

40. J. Sun and C. A. Ullrich, "Optical properties of $CsCu_2X_3$(X=Cl, Br, and I): A comparative study Between hybrid time-dependent density-functional theory and the Bethe-Salpeter equation," *Physical Review Materials* 4 (2020): 095402, https://doi.org/10.1103/PhysRevMaterials.4.095402.

41. Z. Xing, Z. Zhou, G. Zhong, et al., "Barrierless Exciton Self-Trapping and Emission Mechanism in Low-Dimensional Copper Halides," *Advanced Functional Materials* 32 (2022): 2207638, https://doi.org/10.1002/adfm.202207638.

42. S. Fu, J. Ding, H. Lv, et al., "Resonantly Enhanced Hybrid Wannier–Mott–Frenkel Excitons in Organic–Inorganic Van Der Waals Heterostructures," *Advanced Materials* 37 (2025): 2411972, https://doi.org/10.1002/adma.202411972.

43. L. Xu, B. Tian, T. Wang, et al., "Direct Z-Scheme Polymeric Heterojunction Boosts Photocatalytic Hydrogen Production via a Rebuilt Extended π-Delocalized Network," *Energy & Environmental Science* 15 (2022): 5059–5068, https://doi.org/10.1039/D2EE02380F.

44. J. Yan, E. Rezasoltani, M. Azzouzi, F. Eisner, and J. Nelson, "Influence of Static Disorder of Charge Transfer State on Voltage Loss in Organic Photovoltaics," *Nature Communications* 12 (2021): 3642, https://doi.org/10.1038/s41467-021-23975-3.

45. F.-J. Kahle, A. Rudnick, S. Wedler, et al., "Static and Dynamic Disorder of Charge Transfer States Probed by Optical Spectroscopy," *Advanced Energy Materials* 12 (2022): 2103063, https://doi.org/10.1002/aenm.202103063.

46. X. Zeng, C. Yan, Q. Wang, et al., "High Curvature PEDOT:PSS Transport Layer Toward Enhanced Perovskite Light-Emitting Diodes," *Small* 19 (2023): 2304411, https://doi.org/10.1002/smll.202304411.

47. T. J. Savenije, C. S. Ponseca Jr., L. Kunneman, et al., "Thermally Activated Exciton Dissociation and Recombination Control the Carrier Dynamics in Organometal Halide Perovskite," *The Journal of Physical Chemistry Letters* 5 (2014): 2189–2194, https://doi.org/10.1021/jz500858a.

48. H. Cho, S.-H. Jeong, M.-H. Park, et al., "Overcoming the Electroluminescence Efficiency Limitations of Perovskite Light-Emitting Diodes," *Science* 350 (2015): 1222–1225, https://doi.org/10.1126/science.aad1818.

49. S. Lin, Z. Ma, X. Ji, et al., "Efficient Large-Area (81 cm^2) Ternary Copper Halides Light-Emitting Diodes With External Quantum Efficiency Exceeding 13% via Host-Guest Strategy," *Advanced Materials* 36 (2024): 2313570, https://doi.org/10.1002/adma.202313570.

50. J.-J. Wang, L.-Z. Feng, G. Shi, et al., "High Efficiency Warm-White Light-Emitting Diodes Based on Copper–Iodide Clusters," *Nature Photonics* 18 (2023): 200–206, https://doi.org/10.1038/s41566-023-01340-8.

51. T. Hofbeck, U. Monkowius, and H. Yersin, "Highly Efficient Luminescence of Cu(I) Compounds: Thermally Activated Delayed Fluorescence Combined With Short-Lived Phosphorescence," *Journal of the American Chemical Society* 137 (2015): 399–404, https://doi.org/10.1021/ja5109672.

52. X.-L. Chen, R. Yu, X.-Y. Wu, D. Liang, J.-H. Jia, and C.-Z. Lu, "A Strongly Greenish-Blue-Emitting Cu_4Cl_4 Cluster With an Efficient Spin–Orbit Coupling (SOC): Fast Phosphorescence Versus Thermally Activated Delayed Fluorescence," *Chemical Communications* 52 (2016): 6288–6291, https://doi.org/10.1039/C6CC00809G.

53. H. Cui, W. Zhu, Y. Deng, et al., "Lead-Free Organic–Inorganic Hybrid Scintillators for X-Ray Detection," *Aggregate* 5 (2024): 454, https://doi.org/10.1002/agt2.454.

54. S. Yu, J. Xu, W. Zeng, Z. Xiao, and X. Chen, "Perspective on Understanding the Origin of Trapped Exciton in Lead-Halide Perovskite With Broadband Emission," *Advanced Optical Materials* 14 (2026): 02683, https://doi.org/10.1002/adom.202502683.

55. Y. Fu, Q. Zhang, D. Zhang, et al., "Scalable All-Evaporation Fabrication of Efficient Light-Emitting Diodes With Hybrid 2D–3D Perovskite

16163028, 2026, 71, Downloaded from https://advanced.onlinelibrary.wiley.com/doi/10.1002/adfm.77533 by Jilin University, Wiley Online Library on [07/11/2026]. See the Terms and Conditions (https://onlinelibrary.wiley.com/terms-and-conditions) on Wiley Online Library for rules of use; OA articles are governed by the applicable Creative Commons License

Nanostructures," *Advanced Functional Materials* 30 (2020): 2002913, https://doi.org/10.1002/adfm.202002913.

56. Y. Tian, W. Zheng, X. Zhang, et al., "Triple Ligand Engineered Gold Nanoclusters With Enhanced Fluorescence and Device Compatibility for Efficient Electroluminescence Light-Emitting Diodes," *Nano Letters* 23 (2023): 4423–4430, https://doi.org/10.1021/acs.nanolett.3c00725.

57. A. Todinova, L. Contreras-Bernal, M. Salado, et al., "Towards a Universal Approach for the Analysis of Impedance Spectra of Perovskite Solar Cells: Equivalent Circuits and Empirical Analysis," *ChemElectroChem* 4 (2017): 2891–2901, https://doi.org/10.1002/celc.201700498.

58. Q. Wang, Y. Chen, C. Yan, et al., "Molecularly Designing a Passivation ETL to Suppress EQE Roll-off of PeLEDs," *ACS Energy Letters* 8 (2023): 3710–3719, https://doi.org/10.1021/acsenergylett.3c01379.

Supporting Information

Additional supporting information can be found online in the Supporting Information section.

Supporting File: adfm77533-sup-0001-SuppMat.docx.

16163028, 2026, 71, Downloaded from https://advanced.onlinelibrary.wiley.com/doi/10.1002/adfm.77533 by Jilin University, Wiley Online Library on [07/11/2026]. See the Terms and Conditions (https://onlinelibrary.wiley.com/terms-and-conditions) on Wiley Online Library for rules of use; OA articles are governed by the applicable Creative Commons License